An Analytical Electron Microscopy Study of Paraequilibrium Cementite Precipitation in Ultra-High-Strength Steel

G. GHOSH, C.E. CAMPBELL, and G.B. OLSON

To support quantitative design of ultra-high-strength (UHS) secondary-hardening steels, the precipitation of cementite prior to the precipitation of the M_2C phase is investigated using a model alloy. The microstructure of cementite is investigated by transmission electron microscopy (TEM) techniques. Consistent with earlier studies on tempering of Fe-C martensite, lattice imaging of cementite suggests microsyntactic intergrowth of M_5C_2 (Hägg carbide). The concentration of substitutional alloying elements in cementite are quantified by high-resolution analytical electron microscopy (AEM) using extraction replica specimens. Quantification of the substitutional elements in cementite confirms its paraequilibrium (PE) state with ferrite at the very early stage of tempering. The implications of these results are discussed in terms of the thermodynamic driving force for nucleation of the primary-strengthening, coherent M_2C carbide phase. The ferrite-cementite PE condition reduces the carbon concentration in the ferrite matrix with a significant reduction of M_2C driving force. The kinetics of dissolution of PE cementite and its transition to other intermediate states will also influence the kinetics of secondary hardening behavior in UHS steels.

I. INTRODUCTION

THE desired property objectives in a modern ultra-high-strength (UHS) steel are achieved by controlling the kinetics of a series of solid-state phase transformations. These include the martensitic transformation upon quenching from the solution treatment temperature, cementite precipitation prior to secondary hardening, coherent M_2C precipitation giving rise to secondary hardening, and austenite precipitation for dispersed-phase transformation toughening. Depending on the alloy composition, there can be a significant overlap in the kinetics of last three precipitation processes. Developing appropriate models and tools that reflect the synergistic interplay between the various kinetic processes governing microstructural evolution is the cornerstone of the systems approach to alloy design.[1]

In UHS steels, a fully martensitic microstructure ensures a supersaturated state for the precipitation of extremely fine alloy carbides. Although a comprehensive model to predict the kinetics of martensitic transformation is not available, a fully martensitic microstructure can be obtained if the martensite start temperature (M_s) is sufficiently high. A model for predicting M_s for multicomponent ferrous alloys with good accuracy is available.[2,3] Secondary hardening, using coherent M_2C carbides (where M = Mo, Cr, Fe, or V), is exploited in the commercial alloys AERMET100*[4] and AF1410[5,6] to obtain UHS, fracture-resistant alloys. During *stage IV* tempering, coherent M_2C carbides are precipitated in a ferrite matrix. However, the precipitation of metastable cementite precedes the precipitation of M_2C carbides, which, in turn, results in the dissolution of cementite. To achieve the desired high-fracture toughness, tempering must be continued until all the cementite is dissolved,[7] because the undissolved cementite particles serve as sites for microvoid nucleation. To maintain a fine M_2C particle size during cementite dissolution, the growth regime of the M_2C carbide precipitation reaction should be suppressed. The kinetics of M_2C carbide precipitation in high–Co-Ni secondary-hardening steels have been studied using atom probe field-ion microscopy (APFIM), transmission electron microscopy (TEM), and small-angle neutron scattering (SANS) measurements to determine particle size, number density, volume fraction, and composition.[8,9,10] The kinetics of austenite precipitation have also been studied in detail.[4,11,12] The previous analyses of the kinetics of M_2C precipitation assumed the presence of paraequilibrium (PE) cementite, but it has not been experimentally verified. To further improve the strengthening efficiency in these alloys, an improved understanding of the thermodynamic state of cementite and its effect on the precipitation of coherent M_2C carbide is required.

In the context of low-alloy steels, the kinetic theories of diffusional phase transformations are well developed.[13–20] An important feature of these kinetic models is the assumption of local equilibrium at the interface. Depending on the interface velocity during transformation, it is convenient to classify the kinetics into two distinct modes. (1) Partitioning local equilibrium (PLE) is characterized by a low interface velocity while maintaining local equilibrium at the interface. Generally, PLE occurs at low supersaturation and its kinetics is governed by the slow-diffusing species (substitutional elements). The thermodynamic condition for PLE is given by

$$\mu_i^{\alpha} = \mu_i^{\theta} \qquad [1]$$

where μ_i is the chemical potential of element i (equal to C, Co, Cr, Fe, Ni, or Mo), and α and θ are ferrite and ce-

*AERMET100 is a trademark of Carpenter Technology, Redding, PA.

G. GHOSH, Research Assistant Professor, and G.B. OLSON, Professor, are with the Department of Materials Science and Engineering, Robert R. McCormick School of Engineering and Applied Science, Northwestern University, Evanston, IL 60208. C.E. CAMPBELL, formerly Graduate Student, Department of Materials Science and Engineering, Robert R. McCormick School of Engineering and Applied Science, Northwestern University, is Postdoctoral Fellow, Metallurgy Division, National Institute of Standards and Technology, Gaithersburg, MD 20899.

Manuscript submitted February 4, 1998.

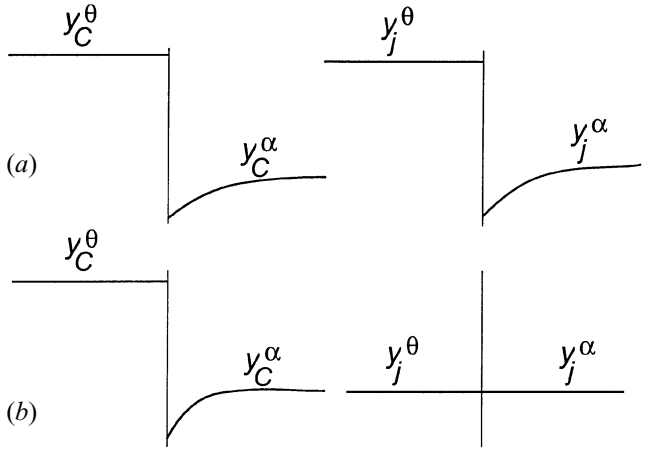

Fig. 1—Schematic composition profiles across the transforming interface associated with (*a*) PLE and (*b*) PE phase transformation involving ferrite (α) and cementite (θ).

mentite, respectively. This condition is also referred to as orthoequilibrium (OE). (2) Paraequilibrium is a kinetically restricted equilibrium when the diffusivity of the substitutional species is negligible compared to that of interstitial species. The presence of PE is defined by a uniform carbon potential and a uniform site fraction of substitutional elements across the transforming interface. In the case of the ferrite-cementite transformation, the thermodynamic conditions for PE are given by

$$\mu_C^\alpha = \mu_C^\theta \qquad [2a]$$

$$y_j^\alpha = y_j^\theta \qquad [2b]$$

$$\Sigma y_j\,(\mu_j^\alpha - \mu_j^\theta) = 0 \qquad [2c]$$

where y_j is the site fraction of substitutional element j (equal to Co, Cr, Fe, Ni, or Mo). For a system containing both substitutional (j) and interstitial (C and/or N) elements, the site fractions are related to the ordinary mole fractions (x):

$$y_j = \frac{x_j}{1 - x_C - x_N} \qquad [3a]$$

$$y_{C\,\mathrm{or}\,N} = \frac{p}{q}\,\frac{x_{C\,\mathrm{or}\,N}}{1 - x_C - x_N} \qquad [3b]$$

According to a two-sublattice model[21] used here, to express the Gibbs energies $p = 1$ and $q = 3$ for ferrite and $p = q = 1$ for austenite.

The schematic concentration profiles across the transforming interface, for the two distinct modes described previously, are shown in Figure 1. The PE nature of phase transformation has been discussed extensively in the context of the kinetics of the austenite-to-ferrite transformation in low-alloy steels. Often the conclusions derived from such an analysis are controversial, due to numerous assumptions involved in the kinetics analysis. On the other hand, since one of the PE conditions is defined in terms of composition (Eq. [2b]), the most conclusive evidence for PE phase transformation can be gathered from high-resolution measurement of the composition of the product phase. As demonstrated earlier by Babu *et al.*,[22] PE transformation is also applicable during precipitation of cementite in ferrite. They studied the partitioning behavior of Mn and Si between cementite and ferrite during tempering in a low-alloy steel by the APFIM technique. Their results suggest that the early stage of cementite growth occurs by the PE mode.

Precipitation of cementite during tempering of martensite in UHS steels also provides an ideal opportunity to study PE phase transformations. As will be shown later, this has a strong bearing on the secondary hardening behavior of UHS steels. Generally, cementite is considered to be stoichiometric with respect to C, or it may exist only over a very narrow range of C concentrations. Thus, one needs to measure the concentration of substitutional elements only. Furthermore, thermochemical data for cementite and ferrite in multicomponent systems of interest are well assessed. These data can be used as a tool for critical analysis of the measured compositions of cementite to validate its thermodynamic state.

The tracer diffusivities of the alloying elements,[23–26] commonly used in UHS steels, in ferrite are listed in Table I at a standard tempering temperature of 783 K. It may be noted that the substitutional elements diffuse about nine to ten orders of magnitude more slowly than carbon. In view of this relatively slow diffusivity, the purpose of the present study is to establish the thermodynamic state of cementite that forms prior to the precipitation of the primary strengthening phase (M_2C carbide). If ferrite-cementite PE prevails at the early stage of tempering, then the site fraction of the substitutional elements in cementite should be exactly the same as that in the starting alloy. To determine the structure and composition of the cementite particles, analytical electron microscopy (AEM) techniques were employed. An unambiguous interpretation of the nature of the ferrite-cementite equilibrium can be made if the composition analysis of cementite in AEM is not affected by the presence of a ferrite matrix. Quantitative X-ray microanalysis in thin foils requires that the precipitate extend through the thickness of the foil. Otherwise, the collected X-ray spectrum may contain contributions from both the precipitate and matrix phases, and the determination of the exact composition of the precipitate becomes difficult. Therefore, to avoid these uncertainties, we have chosen to use extraction replicas only. Besides eliminating the effect of the matrix, the extraction replica technique is very convenient for relatively rapid composition analysis and for collecting statistically significant data. These factors are important in this study, due to the highly dislocated martensitic substructure and heterogeneous nature of cementite precipitation, which make their identification and chemical analysis more time-consuming if thin foil specimens are used.

II. MATERIALS AND EXPERIMENTAL PROCEDURES

The model alloy 1605-2C was used to investigate the initial stages of cementite precipitation. The composition of 1605-2C, listed in Table II, is similar to that of two commercial UHS steels, (the AERMET100 (Redding, PA) and AF1410 alloys), except that it has a lower Ni concentration, which prevents the precipitation of austenite during the later stages of tempering. An experimental 7.7-kg. heat of 1605-2C was produced by Carpenter Technology using vacuum induction melting, with rare-earth additions to getter impurities. The wrought, forged material was solution treated

Table I. Tracer Diffusivities of C, Co, Cr, Ni, and Mo in α-Fe at 783 K

Element	Diffusivity Expression [Ref.] (cm^2/s)	Diffusivity at 783 K (cm^2/s)	D_j/D_C
C	$0.02 \exp\left(-\frac{84{,}139}{RT}\right)$[23]	4.979×10^{-8}	—
Co	$7.19 \exp\left(-\frac{260{,}400}{RT}\right)$ [26]	3.052×10^{-17}	6.13×10^{-10}
Cr	$8.52 \exp\left(-\frac{250{,}800}{RT}\right)$ [24]	1.58×10^{-16}	3.173×10^{-9}
Ni	$1.40 \exp\left(-\frac{245{,}800}{RT}\right)$ [26]	5.597×10^{-17}	1.124×10^{-9}
Mo	$0.44 \exp\left(-\frac{238{,}000}{RT}\right)$ [25]	5.83×10^{-17}	1.171×10^{-9}

R = 8.314 J/mol/K; and T is the temperature in Kelvin.

Table II. Composition of Alloys Studied (in Weight Percent)

Alloy	Fe	Co	Ni	Cr	Mo	C
AF1410	bal	14.0	10.0	2.0	1.05	0.16
AERMET100	bal	13.0	11.0	3.0	1.0	0.24
1605-2C	bal	16.08	4.97	0.71	2.82	0.247

at 1398 K for 1.5 hours in an inert Argon environment. Solution treatment was followed by an oil quench to room temperature. Tempering was performed at 783 K in a molten salt bath for 5, 10, and 15 minutes. After tempering, the material was water quenched to room temperature.

Extraction replicas of heat-treated materials were prepared by depositing a thin carbon film on a polished and etched surface. The carbon film was then floated off the specimens in a solution of 5 pct nitric acid in methanol and collected on palladium-coated copper grids. The extraction replicas were examined by AEM to determine the structure by convergent-beam electron diffraction (CBED) technique and to determine the composition by energy-dispersive (EDS) X-ray microanalysis. High-resolution electron microscopy (HREM) and analytical characterization were performed in a cold-field emission gun high-resolution analytical electron microscope (Hitachi HF-2000) equipped with a Gatan 666 parallel electron energy-loss spectrometry detector, an ultrathin-window Link EDS detector and data processor (QX2000) and a Gatan charge-coupled device camera for HREM imaging. The analytical electron microscope was operated at 200 kV. The take-off angle for the X-ray detector was 68 deg. The X-ray collection time was 120 seconds, and the electron probe size was about 5 nm. Care was taken to ensure that the particle being analyzed was not in a two-beam condition, in order to minimize electron channeling effects.[27] The X-ray spectra were deconvoluted, to separate the overlapping peaks, and the background-subtracted integrated intensities were obtained using Desktop Spectrum Analyzer (DTSA 2.01) software.[28]

Figure 2 shows a typical EDS X-ray spectrum from a plate-shaped cementite particle after 10 minutes of tempering. The background-subtracted integrated intensities of such spectra were converted to compositions by using the following equations:[27]

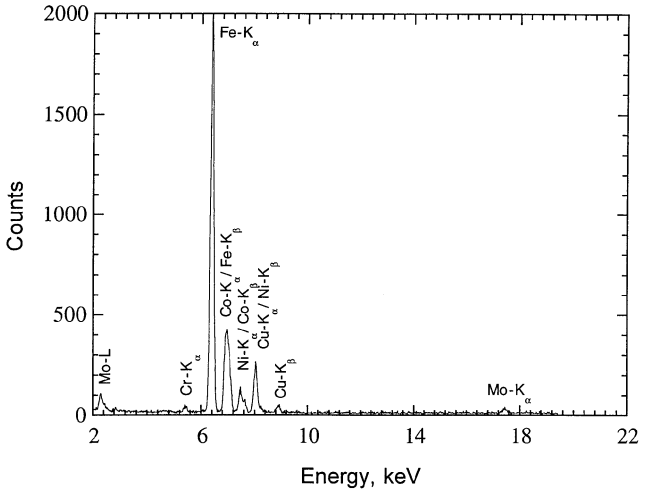

Fig. 2—An as-collected EDS X-ray spectrum from a plate-shaped cementite particle after tempering 1605-2C at 783 K for 10 min. The X-ray collection time was 120 s. Background subtracted integrated intensities were obtained by deconvoluting the peaks using DTSA software.[28]

$$\frac{w_j}{w_{Fe}} = k_{j/Fe}\frac{I_j}{I_{Fe}} \times [ACF] \times \frac{1}{\left(1 + \frac{I^j}{I_j}\right)} \qquad [4]$$

$$w_{Co} + w_{Cr} + w_{Fe} + w_{Ni} + w_{Mo} = 1 \qquad [5]$$

where j = Co, Cr, Ni, and Mo; w_j is the weight fraction (wt fr) of element j (equal to Co, Cr, Ni, and Mo), I_j is the x-ray intensity of element j, I^j/I_j is the ratio of fluorescence intensity to primary intensity, and $k_{j/Fe}$ is the proportionality constant or the Cliff–Lorimer factor.[29] Although there are several ways to evaluate I_j, we have taken I_j to be the background-subtracted integrated intensity of the K_α peak of element j. The $k_{j/Fe}$ factors can be expressed as

$$k_{j/Fe} = \frac{w_j}{w_{Fe}}\frac{I_{Fe}}{I_j} \times \frac{\left(1 + \frac{I^j}{I_j}\right)}{[ACF]} \qquad [6]$$

The absorption correction factor (ACF) is given by[27]

$$\mathrm{ACF} = \left[\frac{\mu/\rho]^{j}_{\mathrm{SPEC}}}{\mu/\rho]^{\mathrm{Fe}}_{\mathrm{SPEC}}}\right] \times \left[\frac{1 - \exp\{-\mu/\rho]^{\mathrm{Fe}}_{\mathrm{SPEC}}(\rho t)\ \mathrm{cosec}\ \alpha\}}{1 - \exp\{-\mu/\rho]^{j}_{\mathrm{SPEC}}(\rho t)\ \mathrm{cosec}\ \alpha\}}\right] \quad [7]$$

$$\mu/\rho]^{j}_{\mathrm{SPEC}} = \mu/\rho]^{j}_{\mathrm{Co}}\, w_{\mathrm{Co}} + \mu/\rho]^{j}_{\mathrm{Cr}}\, w_{\mathrm{Cr}} + \mu/\rho]^{j}_{\mathrm{Fe}}\, w_{\mathrm{Fe}} + \mu/\rho]^{j}_{\mathrm{Mo}}\, w_{\mathrm{Mo}} + \mu/\rho]^{j}_{\mathrm{Ni}}\, w_{\mathrm{Ni}} \quad [8]$$

where ρ is the density, t is the thickness of the sample, and α is the take-off angle of the X-ray detector. The mass-absorption coefficients for the pure elements $\mu/\rho]^{j}_{\mathrm{Co}}$, *etc.*, in Eq. [8] were taken from those listed in Reference 30. The formulation for the fluorescence correction proposed by Nockolds *et al.*[31] was used. Among the elements of interest here, Cr K_α can be fluoresced by Fe K_α, which, in turn, can be fluoresced by Ni K_α. The fluorescence yield of Cr K_α due to Fe K_α is given by[31]

$$\frac{I^{\mathrm{Cr}}}{I_{\mathrm{Cr}}} = w_{\mathrm{Fe}}\omega_{\mathrm{Fe}}\left(\frac{r_{\mathrm{Cr}} - 1}{r_{\mathrm{Cr}}}\right)\frac{A_{\mathrm{Cr}}}{A_{\mathrm{Fe}}}\,\mu/\rho]^{\mathrm{Fe}}_{\mathrm{Cr}}\,\frac{E_{c\mathrm{Cr}}}{E_{c\mathrm{Fe}}} \frac{\ln(E_o/E_{c\mathrm{Fe}})}{\ln(E_o/E_{c\mathrm{Cr}})}\,\frac{\rho t}{2}\,[0.932 - \rho t \ln(\mu/\rho]^{j}_{\mathrm{SPEC}})] \quad [9]$$

where ω_{Fe} is the fluorescence yield of Fe; r_{Cr} is the absorption-jump ratio of Cr; A_{Cr} and A_{Fe} are the atomic weights of Cr and Fe respectively; E_o is the operating voltage, and $E_{c\mathrm{Cr}}$ and $E_{c\mathrm{Fe}}$ are the critical excitation energies for the characteristic radiation of Cr and Fe, respectively. All material parameters needed to evaluate Eq. [9] were taken from Reference 32. Similarly, the fluorescence yield of Fe K_α due to Ni K_α was also calculated. The fluorescence yield due to K_β radiation was neglected.

The $k_{j/\mathrm{Fe}}$ factors were determined using thin foils of two single-phase alloys: Fe-0.23C-14.17Co-10.24Ni-3.96Mo and Fe-0.259C-15.97Co-8.97Cr-4.97Ni (in wt pct). The X-ray spectra were collected from foil thicknesses of 100 nm or less. The foil thickness was determined by CBED.[33] In the aforementioned thickness ranges, Co, Cr, and Ni satisfied the criteria of a thin foil and the ACF correction was employed for Mo. For the second standard alloy, the Cr K_α fluorescence yield was found to be about 3 pct, while that of Fe K_α was found to be negligible.

The statistical accuracy of the composition determination from Eq. [4] is primarily limited by the counting statistics of the X-ray collection process.[27,34] When the X-ray spectra are collected for a sufficiently long time to obtain several thousand counts in each peak, the counting statistics can be assumed to follow a normal distribution. However, in a multicomponent system, it may be difficult to satisfy this criterion for each element if experiments are to be carried out within a reasonable period of time. Nevertheless, since the composition of cementite was determined by analyzing about 30 different particles, the confidence interval is estimated by the statistics of the student t distribution. The total relative error ($\Delta\varepsilon_{w_j}$) in the determination of composition is given by

$$\Delta\varepsilon_{w_j} = \Delta\varepsilon_{k_{j/\mathrm{Fe}}} + \Delta\varepsilon_{I_{j/\mathrm{Fe}}} \quad [10]$$

where $\Delta\varepsilon_{k_{j/\mathrm{Fe}}}$ and $\Delta\varepsilon_{I_{j/I_{\mathrm{Fe}}}}$ are the relative errors associated with k factors and in the counting statistics of X-rays in the specimen of unknown composition, respectively. They are given by[34]

$$\Delta\varepsilon_{k_{j/\mathrm{Fe}}} = \frac{t^{\mathrm{n}-1}_{99}}{\sqrt{n}}\,\frac{\sigma_k}{k_{j/\mathrm{Fe}}}\,100 \quad [11]$$

$$\Delta\varepsilon_{I_{j/I_{\mathrm{Fe}}}} = \frac{t^{\mathrm{n}-1}_{99}}{\sqrt{n}}\,\frac{\sigma_I}{I_j/I_{\mathrm{Fe}}}\,100 \quad [12]$$

where $t^{\mathrm{n}-1}_{99}$ are the student t values for n measurements at a 99-pct confidence level; σ_k and σ_I are the standard deviations for the k factor and intensity ratio measurements, respectively; $k_{j/\mathrm{Fe}}$ is the mean of the n values of the k factor, and $\overline{I_j/I_{Fe}}$ is the mean of the n values of I_j/I_{Fe}. Since the concentrations of only substitutional elements were determined, their site fractions in the metal sublattice are given by the respective atomic fraction. The relationship between the atomic fraction and the weight fraction was used to calculate the total relative error in the former from that in the latter using a standard mathematical procedure.

The OE and the nucleation driving-force calculations were performed using the multicomponent thermodynamic software, Thermo-Calc.[35,36] The PE calculations, between ferrite and cementite, were carried out in the PARROT module[37] of the Thermo-Calc software. In all calculations, the SGTE solution database[38] was used.

III. RESULTS AND DISCUSSION

A. *Microstructure of Precipitated Cementite*

Figure 3 shows bright-field TEM micrographs of the cementite particles in an extraction replica. The cementite particles may be categorized as intra- and interlath types. It is believed that both intra- and interlath cementite particles nucleate heterogeneously, the former in the vicinity of dislocations within the martensite lath and the latter in the martensite lath boundaries. The interlath cementite particles precipitate as laths, having a high aspect ratio (length/width). The intralath particles are somewhat irregular in shape; nonetheless, they were characterized by their lengths and widths. Generally, the intralath cementite particles are smaller than the interlath cementite particles. The distribution of the cementite particles in Figure 3(a) suggests that they are predominantly the interlath type. Evidence of intralath precipitation may also be noticed in Figures 3(a) through (c). Also, the temporal evolution of the cementite particles suggests that they undergo a morphological transition from a lath shape to a plate shape. The average length, width, and aspect ratio of the cementite particles are listed in Table III as a function of tempering time. To evaluate these quantities, the maximum dimension of the particle was taken as the length, and the maximum dimension in a direction perpendicular to the length was taken as the width. Each data set is based on the measurement of about 75 randomly selected cementite particles. In general, the standard deviation in all these measurements is rather high, due to different shapes and dimensions associated with the interlath, intralath, and morphological change of the cementite particles. The micrographs in Figure 3 suggest that the precipitation of cementite continues

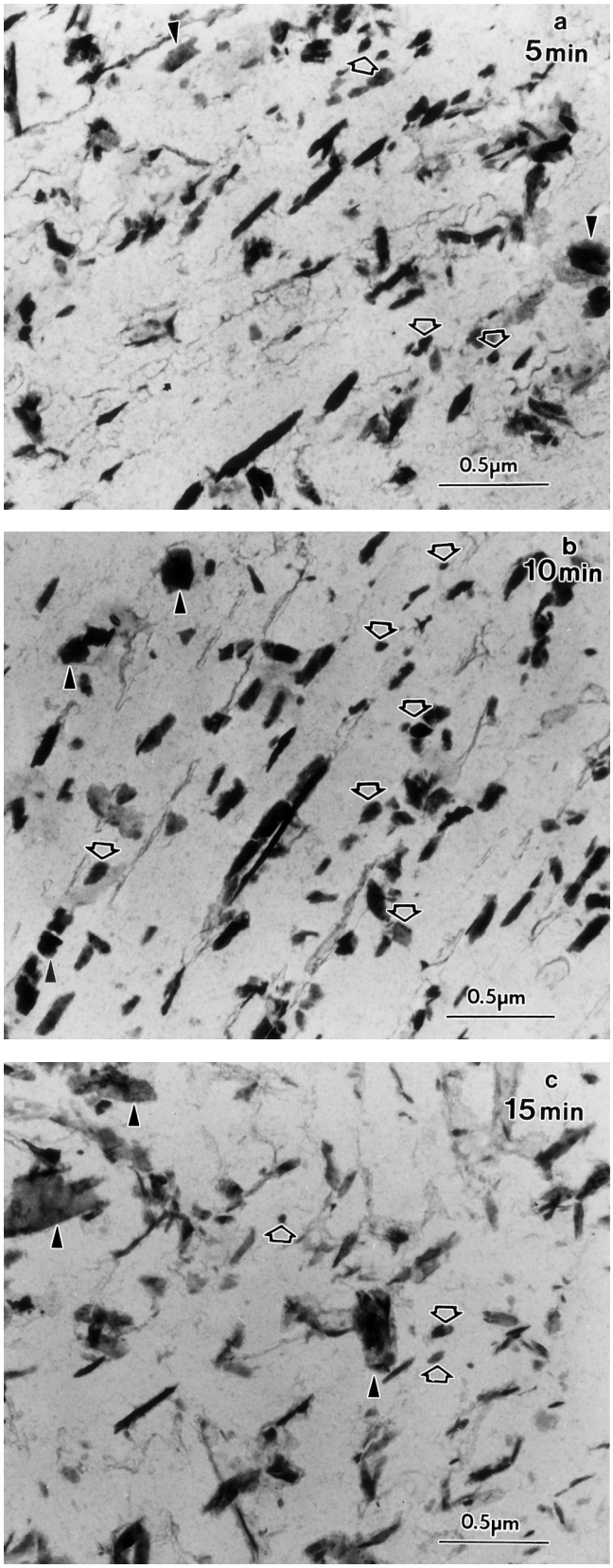

Fig. 3—Bright-field TEM micrographs of the cementite particles, in extraction replica, after tempering alloy 1605-2C at 783 K: (*a*) 5 min, (*b*) 10 min, and (*c*) 15 min. In each micrograph, some of the intralath and lath-shaped cementite particles are shown with open and solid arrows, respectively.

Table III. Dimension of Cementite Particles after Tempering 1605-2C at 783 K

Tempering Time	Average Length (nm)	Average Width (nm)	Average Aspect Ratio
5 min	138.2 ± 72.3	41.2 ± 17.6	3.64 ± 1.85
10 min	169.7 ± 93.2	53.8 ± 22.7	3.67 ± 3.43
15 min	171.6 ± 93.4	46.7 ± 36.2	4.67 ± 1.79

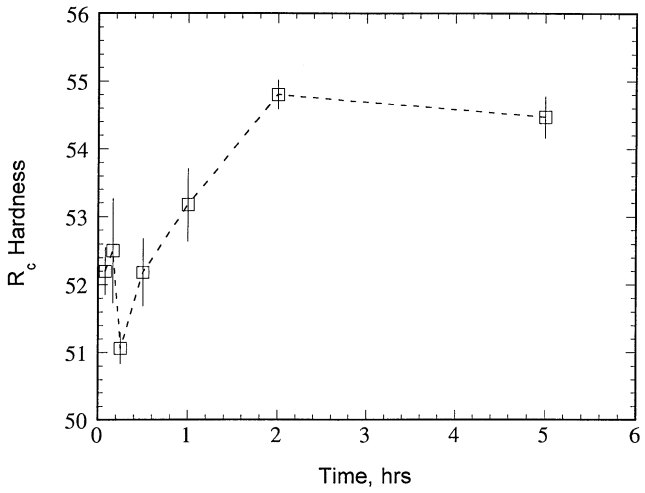

Fig. 4—Ambient hardness of alloy 1605-2C as a function of tempering time at 783 K.

for up to about 10 minutes. This is consistent with the measurement of volume fraction of cementite by Montgomery[6] in a related, commercial UHS steel (AF1410), which was also tempered at 783 K. Montgomery[6] used X-ray diffraction and observed a maximum in volume fraction at around 12 minutes of tempering. The data in Table III suggest that both lengthening and thickening continue up to about 10 minutes of tempering. During this time period, the average aspect ratio remains virtually constant. However, the standard deviation of the average aspect ratio after 10 minutes of tempering is very high. This is most probably due to the following factors: (1) more nucleation of intralath particles, as indicated by Figure 3(b); (2) preferential lengthening of pre-existing interlath particles; (3) coarsening of the particles under PE mode; and (4) morphological transition from lath to plate of some of the interlath particles. After 15 minutes of tempering, while there is only a marginal increase in the average length of the particles, the average width decreases by about 20 pct (compared to that after 10 minutes of tempering), resulting in an increase in the average aspect ratio. The plate-shaped cementite particles can be both inter- and intralath types. Even though several relatively large cementite plates may be noticed in Figure 3(c), the decrease in average width suggests an edgewise dissolution (possibly by a ledge mechanism) of plate-shaped cementite particles. The heterogeneous precipitation and subsequent dissolution of plate-shaped cementite particles are likely promoted by enhanced diffusion along the martensite lath boundaries. The dissolution of cementite is also consistent with the observed secondary hardening behavior shown in Figure 4, where the increase in hardness after 15 minutes of tempering is indicative of precipitation of the coherent M_2C phase. During the secondary hardening pro-

cess, the cementite and M_2C particles act as a ''source'' and ''sink'' for carbon, respectively. However, the extraction replica of the 15-minute tempered sample did not reveal the presence of M_2C particles, implying that either they were not extracted or they were too small (<1 nm).

There is a plethora of experimental studies on the structural changes during tempering of martensitic carbon steels. The structural changes taking place during tempering are classified into three categories: (1) *stage I* precipitation of ε-carbide (around 370 K, 1 hour), (2) *stage II* decomposition of austenite (around 550 K, 1 hour), and (3) *stage III* precipitation of cementite (between 550 and 800 K, 1 hour). The tempering temperature in this study falls in the last range. Even though the final product after *stage III* tempering is cementite (Fe_3C), a question remains if the Hägg carbide (Fe_5C_2) appears at the early stage of *stage III* tempering.[39,40,41] Various experimental techniques have been used to resolve this issue, *e.g.*, magnetometry,[42] Mössbauer spectroscopy,[43] X-ray diffraction,[44] and electron microscopy.[45–50] Due to the very fine scale and highly defective microstructure of the carbides, it has been shown[49,50] that electron diffraction and HREM are more advantageous than X-ray diffraction in resolving the outstanding issues.

The structure of cementite is well established.[51,52,53] It has an orthorhombic structure with the space group *Pnma* (no. 62). The atom positions are given by C ($x = 0.89$, $y = 0.25$, and $z = 0.45$) at 4*c*, Fe1 ($x = 0.186$, $y = 0.063$, and $z = 0.328$) at 8*d*, and Fe2 ($x = 0.036$, $y = 0.25$, and $z = 0.852$) at 4*c*. The lattice parameters are $a = 0.509$ nm, $b = 0.6748$ nm, and $c = 0.4523$ nm.[53] Figure 5 shows a CBED pattern of cementite along $[113]_{ZA}$. Structural factor calculations suggests that ($hh0$) reflections with $h = (2n + 1)$ are forbidden. In Figure 5, they are possibly due to a double diffraction effect. Figure 6 shows a lattice image, taken close to $[2\bar{1}0]_{ZA}$, of plate-shaped cementite formed after 5 minutes of tempering at 783 K. Many planar defects parallel and perpendicular to the lattice fringes may be observed. The latter (shown with white arrows) are likely the growth defects due to end-on collision of the platelets, which are typically 3- to 5-nm thick. Figure 6 suggests that the platelets nucleate independently, but have the same orientation relationship with the matrix. Their rapid radial growth causes end-on coalescence. The other major type of planar defect region is about 1-nm thick. These regions are most likely due to the microsyntactic intergrowth of the Fe_5C_2 Hägg carbide. The stacking mode of cementite can be described by two kinds of prism layers, A and B, which are rotated by 180 deg with respect to each other about the normal of the prism layer.[49] The stacking sequence of cementite is A/B/A/B. . .with a stacking period of 0.34 nm. The structure of Fe_5C_2 can be derived from double prism layers where two kinds of prism layers are linked together by sharing the prism edges. Thus, the stacking sequence of Fe_5C_2 can be expressed as AB/AB/AB/. . . .The structure of higher-order carbides (general formula $Fe_{2n+1}C_n$ and $n > 1$) differs from cementite only in the number of linked prism layers. Thus, they can grow along an axis normal to the stacking plane, giving rise to microsyntactic intergrowth.

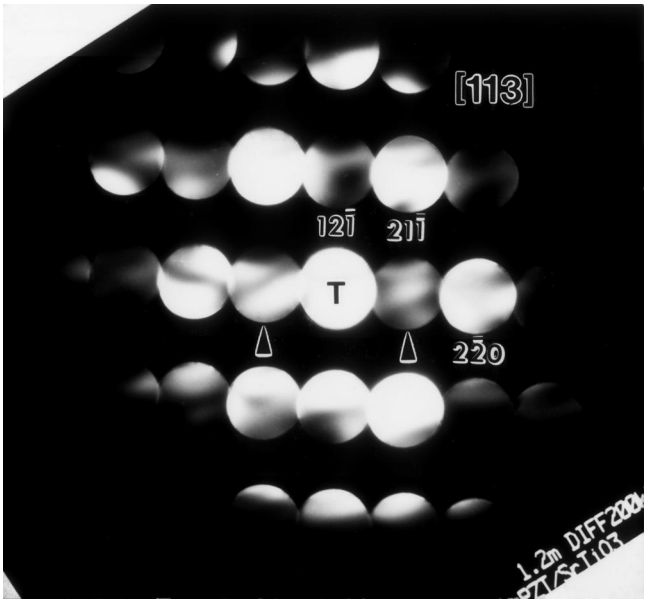

Fig. 5—Convergent beam electron diffraction pattern from a cementite particle along $[113]_{ZA}$.

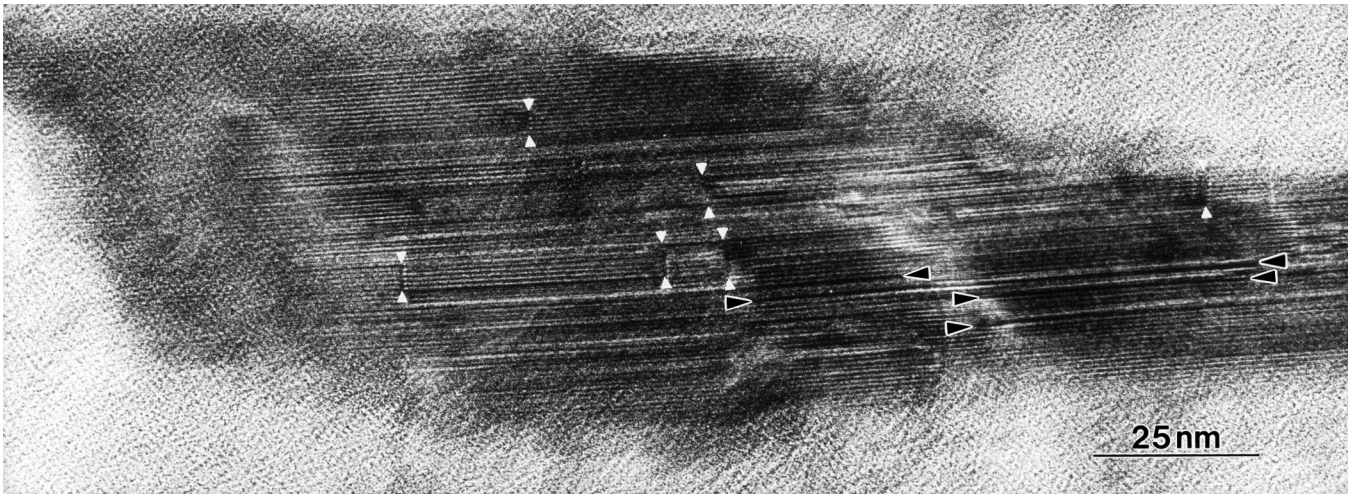

Fig. 6—Lattice image of a plate-shaped cementite particle, formed after 5 min of tempering at 783 K, showing numerous planar defects. The defects perpendicular to the lattice fringes (shown with white arrows) are due to an end-on coalescence of the platelets and the defects parallel to the lattice fringes (shown with dark arrows) are most likely due to microsyntactic intergrowth of Hägg carbide (Fe_5C_2 or M_5C_2).

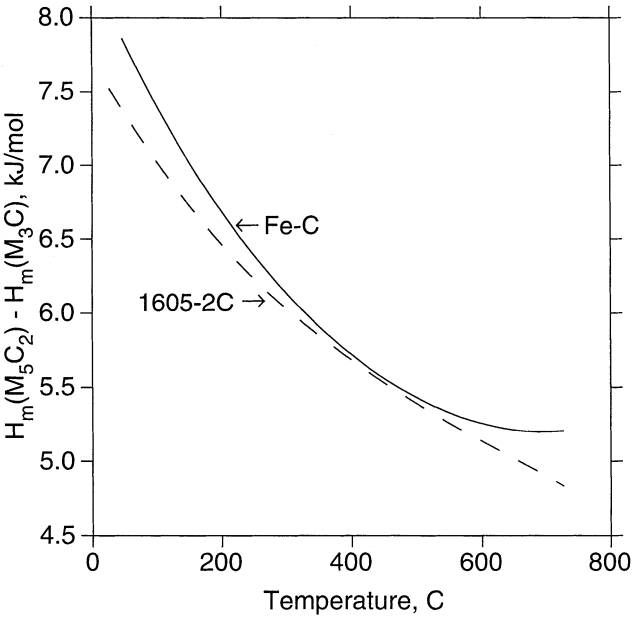

Fig. 7—The difference in enthalpy of formation between the Hägg carbide and cementite. The reference states are graphite-C, hcp-Co, bcc-Cr, bcc-Fe, bcc-Mo, and fcc-Ni. In the case of Fe-C system (shown with solid line), this difference is nothing but $H_m(Fe_5C_2)$-$H_m(Fe_3C)$. For the alloy 1605-2C (shown with dashed line), the difference was calculated using the metal site fractions of the alloy, *i.e.*, $y_{Co} = 0.1562$, $y_{Cr} = 0.0078$, $y_{Fe} = 0.7707$, $y_{Mo} = 0.0168$, and $y_{Ni} = 0.0485$. This figure suggests that the stability of Hägg carbide is not significantly affected by the presence of a substantial amount of the preceding alloying elements.

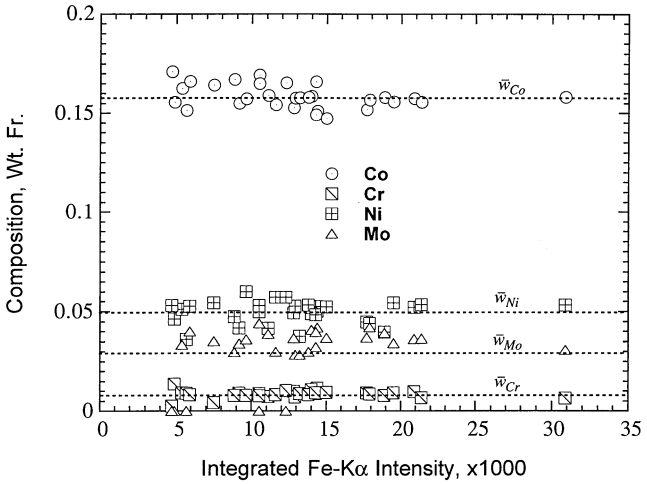

Fig. 8—The distribution of concentrations (in wt fr.) of Co, Cr, Mo, and Ni, as a function of integrated intensity of Fe, after tempering alloy 1605-2C for 5 min at 783 K. Horizontal lines indicate the average composition.

Depending on the tempering temperature, microsyntactic growth of several higher-order carbides within cementite is possible. However, it is believed that, above approximately 673 K, only Fe_5C_2 intergrows within cementite.[50] Figure 6 also suggests the presence of a stacking disorder within the cementite regions. All these observations are consistent with the faulted cementite structure reported earlier.[49]

The stability of cementite and higher-order carbides is affected by their composition. Figure 7 compares the difference in enthalpy of formation between the Hägg carbide (M_5C_2) and cementite (M_3C) in the Fe-C system and in the 1605-2C alloy, using the assessed thermochemical data.[38] For the Fe-C system (solid line), this difference is simply $H_m(Fe_5C_2)$-$H_m(Fe_3C)$. For the 1605-2C alloy (dashed line), the enthalpy difference was calculated using the site fractions of its metal constituents, *i.e.*, $y_{Co} = 0.1562$, $y_{Cr} = 0.0078$, $y_{Fe} = 0.7707$, $y_{Mo} = 0.0168$, and $y_{Ni} = 0.0485$. Figure 7 shows that, at 783 K, the relative stability of the Hägg carbide remains virtually unaffected by the presence of substantial amounts of alloying elements. Furthermore, even though cementite is more stable than the Hägg carbide, the microsyntactic intergrowth of the latter may be promoted by interfacial matching, similar to the role of stacking faults in ε-carbide plates.[54] The tempering studies of Fe-C martensite by Nagakura *et al.*[49,50] indicate that the frequency and extent of microsyntactic intergrowth of the Hägg carbide in cementite is a function of aging tempera-

Table IV. The Calculated Metal Site Fractions in Cementite in the Orthoequilibrium and Paraequilibrium States with Ferrite Are Compared with Those Measured after 5, 10, and 15 Minutes of Tempering the 1605-2C at 783 K*

	Site Fractions of Constituents in Metal Sublattice in Cementite				
	Co	Cr	Fe	Ni	Mo
Orthoequilibrium (Eq. [1])	0.0324	0.1912	0.6131	0.0229	0.1403
Paraequilibrium (Eq. [2])	0.1562	0.0078	0.7707	0.0485	0.0168
Measured after					
5 min at 783 K	0.1523 ± 0.0123 (0.1571 ± 0.0092)	0.0093 ± 0.0012 (0.0085 ± 0.0010)	0.7725 (0.7551)	0.0482 ± 0.0053 (0.0495 ± 0.0044)	0.0177 ± 0.0062 (0.0297 ± 0.0066)
10 min at 783 K	0.1523 ± 0.0091 (0.1571 ± 0.0064)	0.0083 ± 0.0016 (0.0076 ± 0.0014)	0.7751 (0.7578)	0.0466 ± 0.0055 (0.0479 ± 0.0047)	0.0176 ± 0.0056 (0.0296 ± 0.0061)
15 min at 783 K	0.1412 ± 0.0110 (0.1444 ± 0.0074)	0.0161 ± 0.0025 (0.0146 ± 0.0021)	0.7630 (0.7394)	0.0480 ± 0.0056 (0.0489 ± 0.0044)	0.0316 ± 0.0123 (0.0526 ± 0.0131)

*The measured weight fractions of the metal constituents in cementite are shown in parentheses. The uncertainties correspond to the total error (Eq. [10]) at 99 pct confidence level. The metal site fractions in the starting alloy are $y_{Co} = 0.1562$, $y_{Cr} = 0.0078$, $y_{Fe} = 0.7707$, $y_{Mo} = 0.0168$, and $y_{Ni} = 0.0485$.

ture. This is consistent with our observation of fewer and thinner intergrowth regions than those reported by Nagakura *et al.*

B. *Composition of Precipitated Cementite*

The k factors used in this study were $k_{Co/Fe} = 1.0423 \pm 0.0232$, $k_{Cr/Fe} = 0.8457 \pm 0.0213$, $k_{Ni/Fe} = 1.0725 \pm 0.0338$, and $k_{Ni/Fe} = 2.8287 \pm 0.2903$. During X-ray spectra collection, the thickness of each cementite particle analyzed was not determined. However, the thickness of a few of the large particles analyzed was found to lie in the range of 50 to 60 nm. In this thickness range, the ACF for Mo is about 2 pct. The fluorescence yields for Cr K_α and Fe K_α were negligible. Figure 8 shows the distribution of concentrations of Co, Cr, Mo, and Ni in cementite, after 5 minutes of tempering, as a function of Fe K_α counts. For each heat treatment, about 30 cementite particles were randomly selected and the X-ray spectra were collected. Even though many of these data represent cementite particles having different thicknesses, it is important to bear in mind that, in a field-emission microscope, a higher count does not necessarily imply a higher thickness of the specimen being analyzed. The measured metal-site fractions of the various constituents as a function of heat treatment, with the error bar at a 99-pct confidence level, are listed in Table IV. The site fractions of Co, Cr, Fe, Mo, and Ni in the 1605-2C, alloy are 0.1562, 0.0078, 0.7707, 0.0168, and 0.0485, respectively. As seen in Table IV, these values match very well with the measured average compositions after 5 and 10 minutes of tempering. As one would expect, the major source of relative error of the measured quantities is due to the counting statistics, *i.e.*, Eq. [12]. It accounts for 50 pct or more of the total relative error. Even though the data in Table IV are based on random selection of the cementite particles during chemical analysis, an experiment was also carried out where intralath and interlath cementite particles (25 each) were analyzed separately after 10 minutes of tempering. The average metal-site fractions in this experiment were found to be the same, within experimental error, as that of a random analysis. Hence, the initial composition (or thermodynamic state) of precipitated cementite is not affected by the heterogeneous nucleation site.

After 15 minutes of tempering, the measured metal-site fractions indicate a slight, but systematic, departure from the PE state, indicating an intermediate thermodynamic state of the cementite particles. To check if the measured composition differences after 10 and 15 minutes of tempering are statistically meaningful, a student t test was carried out. The t value for two sets of measurements, with average compositions of $\overline{w}_{j,1}$ and $\overline{w}_{j,2}$ based on n_1 and n_2 measurements, is given by[55]

$$t = \frac{|\overline{w}_{j,1} - \overline{w}_{j,2}|}{\sqrt{\sigma_p^2 \left(\frac{1}{n_1} + \frac{1}{n_2}\right)}} \qquad [13a]$$

$$\sigma_p^2 = \frac{(n_1 - 1)\,\sigma_1^2 - (n_2 - 1)\,\sigma_2^2}{n_1 + n_1 - 2} \qquad [13b]$$

where σ_1 and σ_2 are the standard deviations calculated from the total error (Eq. [10]). If the observed value of t is greater than 2.5, the observed difference between $\overline{w}_{j,1}$ and $\overline{w}_{j,2}$ is statistically significant at a 99-pct confidence level. The calculated t values for Co, Cr, Mo, and Ni were 3.93, 4.53, 5.22, and 0.358. This suggests that the observed composition differences for Co, Cr, and Mo are statistically significant at a 99-pct confidence level. Even though the t value for the composition difference of Ni is statistically insignificant, this does not preclude the possibility of an intermediate thermodynamic state, due to the multicomponent nature of the system.

C. *Thermodynamic Analysis of Cementite Precipitation*

Since the site fractions of metal constituents in precipitated cementite are found to be almost identical to those in the starting alloy, this defines the PE thermodynamic state between ferrite and cementite. The SGTE thermochemical database[38] for multicomponent systems, as implemented in the Thermo-Calc (version K) software,[35,36] is used in the present analysis. The phases of interest are ferrite, cementite, and M_2C carbide. During the course of standard tempering practice, only the latter two carbides form. Even though they are not the most stable phases, their formation is kinetically favored. The equilibrium carbides, such as $M_{23}C_6$, M_6C, and M_7C_3, form only after prolonged aging. Therefore, to understand the precipitation process at the initial stages of tempering, we will restrict our thermodynamic calculations to the cementite and M_2C phases only. These phases are described by a two-sublattice model[21,56] where the substitutional elements occupy one sublattice and carbon interstitials occupy the second sublattice. Vacancy interstitials also occupy the second sublattice of the ferrite and M_2C phases. The molar Gibbs energy of a phase ϕ is given by

$$G_m^\phi = G^{ref} + G^{idealmixing} + G^{excess} + G^{magn} \qquad [14a]$$

$$G^{ref} = \sum_M \sum_I y_M y_I G_{M:I}^{0,\phi} \qquad [14b]$$

$$G^{idealmixing} = RT\left[p\left(\sum_M y_M \ln y_M\right) + q\left(\sum_i y_i \ln y_i\right)\right] \qquad [14c]$$

$$G^{excess} = y_j y_k \left[L_{jk}^0 + (y_j - y_k)\, L_{jk}^1 + (y_j - y_k)^2\, L_{jk}^2 + \ldots\right] \qquad [14d]$$

$$G^{magn} = RT \ln(\beta + 1)\, f(\tau) \qquad [14e]$$

where M and I are the substitutional and interstitial elements, respectively; y_M and y_I equal the site fractions on the two sublattices; p and q are the number of sites on each sublattice (for the M_2C phase, $p = q = 1$ and, for ferrite, $p = 1$ and $q = 3$); L is a temperature-dependent parameter describing the excess Gibbs energy; β is the composition-dependent average magnetic moment; $f(\tau)$ is expressed as a polynomial[57] with $\tau = T/T_c$; and T_c is the critical temperature for magnetic ordering.

The site fractions of the constituents in the metal sublattice of cementite are calculated for two distinct thermodynamic states: (1) OE with ferrite, *i.e.*, satisfying Eq. [1],

and (2) PE with ferrite, *i.e.*, satisfying Eq. [2]. The calculated results for the 1605-2C alloy at 783 K are listed in Table IV along with the measured values. The calculated site fractions in the OE state show a very strong departure from those in the PE state, for all constituents. The experimentally measured values after 5 and 10 minutes of tempering match very well with those calculated for the PE state. These results confirm the PE nature of cementite precipitated at the early stage of tempering. Even though OE is the lowest-energy state, there is a significant chemical driving force for the precipitation of cementite in the PE mode. This is given by

$$\Delta G_m^{\alpha\to\theta} = G_m^{\theta} - G_m^{\alpha} + (y_C^{\alpha} - y_C^{\theta}) \frac{\partial G_m^{\theta}}{\partial y_C^{\theta}} \qquad [15]$$

Coates[17,18,19] performed a critical analysis of growth in the PE mode in ternary systems, for precipitates of three geometries with characteristic dimensions. He has argued that, even in the absence of partitioning of substitutional elements, it is difficult to determine determine if a given alloy transforms *via* the PE mode.[19] This is primarily due to the fact that the PE state is very far-removed from local equilibrium; thus, an infinite number of undefined nonequilibrium states may exist between local equilibrium and PE.[58] To resolve this issue, Coates[17,19] proposed an arbitrary criterion based on the width of the interface ''spike'' for element *j*, in order to distinguish between PE and no-partition local equilibrium. If the width of the interface spike is above 5 nm, the local equilibrium condition would be maintained, and, if it is below 1 nm, the PE mode will be operational. Based on the average width and length measurements of cementite particles after 5 and 10 minutes of tempering, the average thickening and lengthening velocities are estimated to be 0.042 and 0.105 nm/s, respectively. Since the aspect ratio of the cementite plates remains practically constant for up to 10 minutes of tempering, the growth behavior of the cementite particles can be described by the lengthening velocity of the interface. As shown in Table I, among the substitutional elements, Cr is the fastest-diffusing species. Using the D_{Cr} value listed in Table I and the aforementioned lengthening velocity, the width of the interface spike[14,17,19,59] is calculated to be 0.3 nm; thus, it satisfies the criterion for PE growth proposed by Coates.

An alternative approach may be to employ the mechanistic model of solute trapping developed by Aziz.[60] Although this model was originally developed to rationalize nonequilibrium solidification, it can also be extended to solid-solid phase transformations. The central idea behind solute trapping is that when the interface velocity is greater than the diffusional velocity, the solute atoms will be trapped behind the advancing interface. The extent of solute trapping is determined by the magnitude of the interface velocity relative to the diffusional velocity. The former should be much greater than the latter for complete solute trapping. Since the PE growth mode can be conceived as the complete solute trapping in the substitutional sublattice, a comparison between diffusional velocities of the substitutional species and the interface velocity is needed. According to Aziz, the diffusional velocity (u_d) is given by

$$u_d = \frac{D_j}{\lambda} \qquad [16]$$

where D_j is the diffusivity of a substitutional element *j* and λ is the characteristic diffusion distance (taken as 0.2494 nm, or the nearest-neighbor distance of the bcc lattice). With $D_{Cr} = 1.58 \times 10^{-20}$ m^2/s, we obtain $u_d = 0.0633$ nm/s. In other words, the observed average interface velocity (0.105 nm/s between 5 and 10 minutes of tempering) is greater than the diffusional velocity of the fastest-diffusing substitutional species; hence, the observed PE condition is qualitatively consistent with the criteria of solute trapping. It is worth pointing out that we have used the tracer diffusivity of Cr in bcc-Fe rather than its chemical diffusivity in the alloy. Furthermore, since we have considered the fastest-diffusing substitutional species, the calculated diffusional velocity should be considered to be an absolute upper-bound value, while the interface velocity is a lower-bound value, as it was evaluated between 5 and 10 minutes of tempering. The micrographs in Figure 3 suggest that the interface velocity will be much higher at tempering times less than 5 minutes.

After 15 minutes of tempering, the average composition of cementite, listed in Table IV, suggests a small, but systematic, deviation from the PE state. The transition process from PE to OE can be complex.[59] The apparent shift from PE mode is probably due to impingement of the diffusion fields from various particles and the reduction in interface velocity. Hillert[59] suggested that a finite transition range exists between the lower limiting interface velocity for PE and the upper limiting velocity for OE. The width of this transition is determined by interface reaction kinetics and diffusion rates within the interface. A further complication arises during the PE to OE transition, in the class alloy studied here, due to the concomitant precipitation of the coherent M_2C phase. To gain a better understanding of the PE to OE transition, a diffusional simulation, similar to the dissolution of cementite in austenite,[61,62] would be useful. However, such a simulation could not be undertaken, as the temperature dependence of the mobilities of Fe, Co, Mo, Cr, and C in cementite have not been assessed yet. At present, the available mobility parameters are based on the experimental data at 1183 K only.[61]

D. *Implication of PE Cementite Precipitation in UHS Steels*

The AEM characterization of cementite in the 1605-2C alloy after short tempering times at 783 K confirms its PE state with ferrite. This imposes certain restrictions at the onset of the coherent M_2C precipitation process. As shown in Table V, the precipitation of PE cementite significantly reduces the matrix carbon content in three different UHS alloys. It may also be noted in Table V that the formation OE cementite reduces the C content in the matrix even further. These results are similar to the effect of other constrained equilibria, such as the effect of stress on a two-phase equilibrium where an increase in solid solubility of the matrix is generally predicted, compared to the relaxed or unstressed state. To demonstrate the effect of alloying elements on the residual carbon content, a series of PE calculations (*i.e.*, satisfying Eq. [2]) were performed in the Co-Ni space for fixed Cr and Mo contents of 0.71 and 2.82 wt pct, respectively. Figure 9 shows the residual carbon content (in wt fr. x 10^5) in the matrix, after precipitation of PE cementite at 783 K, as a function of the initial Co

Table V. The Carbon Content (in Weight Percent) in Ferrite in the Orthoequilibrium and Paraequilibrium States with Cementite, Compared with the ''As-Quenched'' (Fully Supersaturated) Value

	As-Quenched	After Ferrite-Cementite Paraequilibrium	After Ferrite-Cementite Orthoequilibrium
AF1410	0.16	0.0031	0.00015
AERMET100	0.24	0.0033	0.00011
1605-2C	0.247	0.0041	0.00089

Table VI. Degree of Supersaturation for Homogeneous Nucleation after Ferrite-Cementite Paraequilibrium

Alloy	r^*_{hom}, Å	ΔW^*_{hom}	δ_{hom}
AF1410	14.3	6.75×10^{-19}	0.10
AERMET100	17.1	1.45×10^{-18}	0.09
1605-2C	12.1	7.48×10^{-19}	0.12

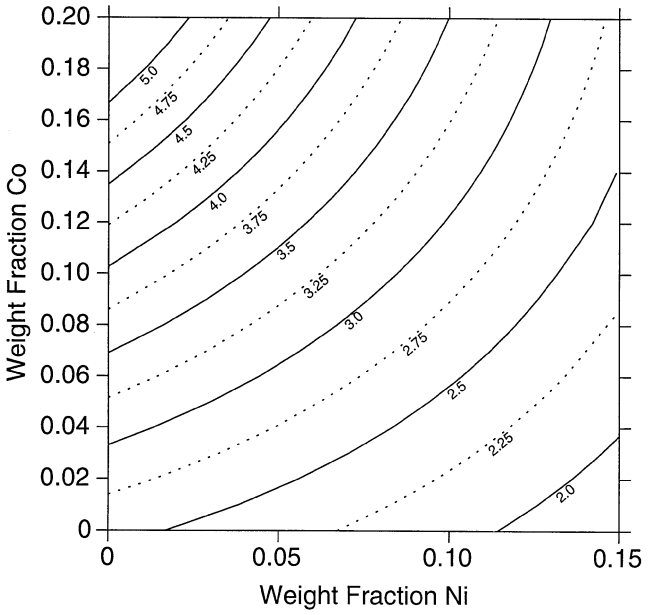

Fig. 9—Contour plot of calculated carbon content (in wt fr. $\times 10^5$) in the matrix, after precipitation of paraequilibrium cementite at 783 K, as a function of alloy Co and Ni content. The Cr and Mo contents were fixed at 0.71 and 2.82 wt pct, respectively.

and Ni content in the alloy. These levels correspond to the solubility limit of carbon in ferrite with respect to PE cementite at 783 K. The curvature of the surface shown in Figure 9 suggests a nonlinear effect of the Co and Ni content in the alloy. A higher Co content and a lower Ni content are beneficial for maximizing the residual carbon content in the ferrite matrix after precipitation of PE cementite.

To ensure a very-fine-scale dispersion of M_2C precipitates (for maximizing strength), it is necessary to maximize the driving force for its coherent nucleation. To model the coherency effects on the nucleation and growth of the M_2C carbides, the composition-dependent elastic energy and the composition-independent interfacial energy terms are added to the free energy of the M_2C phase. An implicit assumption is that the elastic energy is independent of volume fraction, which is not unreasonable at the low volume fractions of

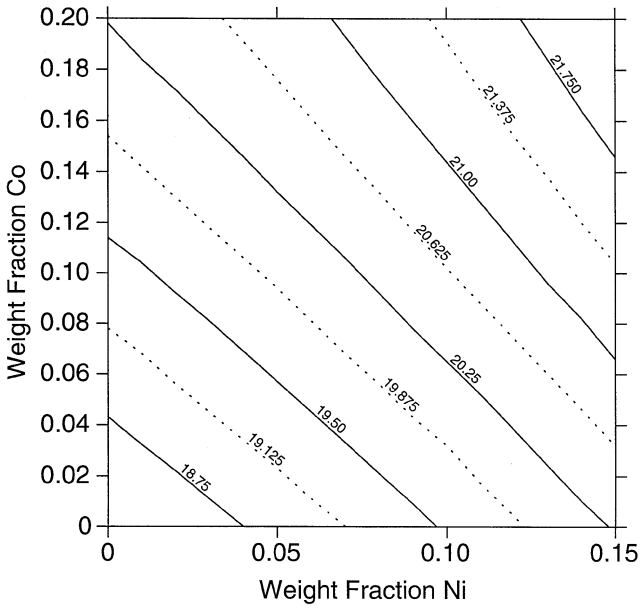

Fig. 10—Contour plot of driving force (in kJ/mol) for the precipitation of coherent M_2C from fully supersaturated ferrite as a function of Co and Ni content at a tempering temperature of 783 K. The C, Cr, and Mo contents were fixed at 0.247, 0.71, and 2.82 wt pct, respectively.

the coherent precipitates. Thus, the molar Gibbs energy of M_2C is given by

$$G_m^{M_2C} = G_m^{Chemical} + G_m^{Elastic} + G_m^{Interfacial} \quad [17]$$

The elastic strain energy is a function of the ferrite and M_2C lattice parameters and the ferrite and M_2C elastic moduli. The linear-elastic strain energy associated with an inhomogeneous inclusion as a function of lattice parameters and shear moduli has been determined by Liarng.[63] For the alloy M_2C carbides, the compositional dependence of the lattice parameters and shear moduli has been investigated by Knepfler.[64] Combining the work of Liarng and Knepfler, the compositional- dependent elastic strain energy was expressed as Redlich–Kister polynomials.[65] By fitting the available M_2C particle-size data from SANS measurements,[8,10] the ferrite-M_2C coherent interfacial energy in a high–Ni-Co secondary-hardening steel was determined to be 120 mJ/m^2.[65] The driving force for precipitation of the coherent M_2C phase is given by

$$\Delta G_m^{\alpha \to M_2C} = G_m^{M_2C} - G_m^{\alpha} + \sum_i (y_i^{\alpha} - y_i^{M_2C}) \frac{\partial G_m^{M_2C}}{\partial y_i^{M_2C}} \quad [18]$$

Figure 10 shows isodriving-force contours for the precipitation of coherent M_2C, as a function of Co and Ni content in the alloy at 783 K, with the assumption of fully supersaturated ferrite. The C, Cr, and Mo contents were fixed at 0.247, 0.71, and 2.82 wt pct, respectively. This is a rather flat surface, showing a linear increase in driving force with increasing Co and Ni contents in the alloy. However, the scenario is significantly different when the effect of PE cementite is taken into account. Figure 11 shows the isodriving-force contours for the precipitation of coherent M_2C, as a function of the Co and Ni content in the alloy at 783 K, after precipitation of PE cementite, *i.e.*, taking into account the reduced matrix carbon content shown in Figure 9. The important features in Figure 11 to be noted

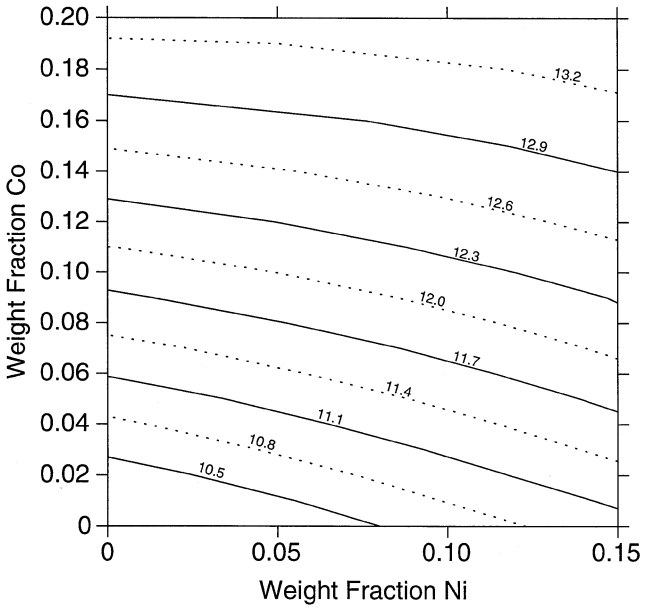

Fig. 11—Contour plot of driving force (in kJ/mol) for the precipitation of coherent M_2C, after precipitation paraequilibrium cememtite, as a function of Co and Ni content at a tempering temperature of 783 K. The Cr and Mo contents were fixed at 0.71 and 2.82 wt pct, respectively. The carbon content in the matrix correponds to that shown in Fig. 9.

are that (a) there is a reduction in the driving force by about 40 pct compared to the values shown in Figure 10, (b) the driving-force surface is no longer flat, and (c) the isodriving-force contours are rotated with respect to those in Figure 10. The latter two features originate from the curvature of the matrix carbon content surface shown in Figure 9.

Assuming that precipitation occurs in the high-supersaturation regime, the particle size of the M_2C carbides can be estimated using the Gibbs–Thomson relation,

$$r^* = \frac{2\gamma}{\Delta G_m^{\alpha \rightarrow M_2C}} \quad [19]$$

where r^* is the particle radius, and γ is the interfacial energy (equal to 120 mJ/m^2). As the strength is maximized by reducing the interparticle spacing, it is advantageous to maximize $\Delta G_m^{\alpha \rightarrow M_2C}$. Since the reduction of C in the ferrite matrix (Table V) significantly reduces the precipitation driving force for M_2C carbides, accurate strength predictions must account for the reduction of coherent M_2C driving force due to the precipitation of PE cementite.

For precipitation in homogeneous solutions, Langer and Schwartz[66] predicted that the growth regime is suppressed when the degree of supersaturation (δ) is greater than 0.3, where δ is defined by

$$\delta = \left[\frac{\kappa T}{\Delta W^*}\right]^{1/2} \quad [20]$$

with κ being the Boltzman constant and ΔW^* being the nucleation barrier height, defined for a homogeneous nucleation as $4/3\pi r^2\gamma$. Applying this criteria, with the use of the Gibbs–Thomson relation (Eq. [19]), to the 1605-2C and AF1410 alloys (Table VI), the observed repressed growth regime is not predicted. This discrepancy between the model predictions and the experimental observations can be accounted for by the observations made by Montgomery[6] and Allen *et al.*[8] indicating that M_2C particles nucleate heterogeneously on dislocations. When the degree of supersaturation for the AF1410 alloy is estimated by calculation of ΔW^* (3.29×10^{-20} to 6.07×10^{-20} J/mol) from heterogeneous nucleation rates, then δ ranges from 0.3 to 0.6.[63]

Even though the PE state of cementite is confirmed by quantifying the substitutional elements in cementite in AEM, the best experimental technique for studying this phase transformation will be the APFIM. By the APFIM technique, it is possible to quantify both substitutional and interstitial elements in ferrite and cementite and also the diffusion spike, if any, at the interface. However, as shown in Figure 3, due to the relatively large size scale and heterogeneous nature of the cementite particles, it will be difficult to perform APFIM. An earlier study used the APFIM technique to determine the partitioning of substitutional elements during tempering of a low-alloy steel;[22] however, the cementite particles were about 6 to 7 times smaller than those shown in Figure 3.

IV. CONCLUSIONS

The confirmation of PE cementite formation prior to coherent M_2C precipitation during tempering provides further insight into the modeling of the strengthening kinetics in UHS steels during secondary hardening. The initial ferrite-cementite PE condition reduces the M_2C driving force significantly, limiting the maximum strength achievable by the alloy. With the ferrite-cementite PE as the initial condition for precipitation of coherent M_2C particles, it leads to fundamental questions regarding how the system evolves from PE to other thermodynamic states, on one hand, and nucleation of coherent M_2C carbide and its coarsening, on the other hand. Alloying elements that retard the formation of PE cementite would be beneficial for maximizing the driving force for precipitation of M_2C carbides. Despite the reduction in driving force, a high dimensionless supersaturation is obtained when the reduced nucleation barrier associated with heterogeneous nucleation is taken into account. This accounts for observed high supersaturation precipitation behavior with suppressed growth.

ACKNOWLEDGMENTS

This work was supported by the National Science Foundation under Grant No. DMR-9500122, the Army Research Office under Grant No. DAAH04-96-1-10266, and the National Science Foundation Graduate Fellowship (CEC).

REFERENCES

1. G.B. Olson: *Science*, 1997, vol. 277, pp. 1237-42.
2. G. Ghosh and G.B. Olson: *Acta Metall. Mater.*, 1994, vol. 42, pp. 3361-70.
3. G. Ghosh and G.B. Olson: *Acta Metall. Mater.*, 1994, vol. 42, pp. 3371-79.
4. C.J. Kuehmann: Ph.D. Thesis, Northwestern University, Evanston, IL, 1994.
5. P.M. Machmeier, C.D. Little, M.H. Horowitz, and R.P. Oates: *Met. Technol.*, 1979, vol. 6, pp. 291-96.
6. J. Montgomery: Ph.D. Thesis, Northwestern University, Evanston, IL, 1990.

7. G.R. Speich, D.S. Dabkowski, and L.F. Porter: *Metall. Trans.*, 1973, vol. 4, pp. 303-15.
8. A.J. Allen, D. Gavillet, and J.R. Weertman: *Acta Metall. Mater.*, 1992, vol. 41, pp. 1869-84.
9. J.S. Montgomery and G.B. Olson: *Proc. 34th Army Sagamore Conf. on Innovations in Ultrahigh-Strength Steel in Technology*, Lake George, NY, 1987, M. Azrin. G.B. Olson, and E.S. Wright, eds., U.S. Government Printing Office, Washington, DC, 1990, pp. 147-78.
10. P. Jemain and J.R. Weertman: Northwestern University, Evanston, IL, unpublished research, 1992.
11. G. Haidemenopoulos, G.B. Olson, and M. Cohen: in *Proc. 34th Army Sagamore Conf. on Innovations in Ultrahigh-Strength Steel in Technology*, Lake George, NY, 1987, M. Azrin, G.B. Olson, and E.S. Wright, eds., U.S. Government Printing Office, Washington, DC, 1990, pp. 549-93.
12. H.E. Lippard: Ph.D. Thesis, Northwestern University, Evanston, IL, 1997.
13. A. Hultgren: *Jernkontorets Ann.*, 1951, vol. 135, p. 403.
14. M. Hillert: Internal Report, Swedish Institute for Metals Research, Stockholm, 1953.
15. J.S. Kirkaldy: *Can J. Phys.*, 1958, vol. 36, pp. 899-925.
16. G.R. Purdy, D.H. Weichert, and J.S. Kirkaldy: *Trans. AIME*, 1964, vol. 230, pp. 1025-34.
17. D.E. Coates: *Metall. Trans.*, 1972, vol. 3, pp. 1203-12.
18. D.E. Coates: *Metall. Trans.*, 1973, vol. 4, pp. 1077-86.
19. D.E. Coates: *Metall. Trans.*, 1973, vol. 4, pp. 2313-25.
20. H.K.D.H. Bhadeshia: *Progr. Mater. Sci.*, 1985, vol. 29, pp. 321-86.
21. M. Hillert and L.-I. Staffansson: *Acta Chem. Scand.*, 1970, vol. 24, pp. 3618-26.
22. S.S. Babu, K. Hono, and T. Sakurai: *Metall. Mater. Trans. A*, 1994, vol. 25A, pp. 499-508.
23. C. Wert: *Phys. Rev.*, 1950, vol. 79, pp. 601-05.
24. A.W. Bowen and G.M. Leak: *Metall. Trans.*, 1970, vol. 1, pp. 1695-1700.
25. A.T. Davenport and R.W.K. Honeycombe: *Met. Sci.*, 1975, vol. 9, pp. 201-08.
26. *Smithells Metals Reference Book*, 7th ed., E.A. Brandes and G.B. Brook, eds., Butterworth-Heinemann Ltd., Oxford, United Kingdom, 1992, p. 13.20.
27. J.I. Goldstein, D.B. Williams, and G. Cliff: in *Principles of Analytical Electron Microscopy*, D.C. Joy, A.D. Romig, Jr., and J.I. Goldstein, eds., Plenum Press, New York, NY, 1986, pp. 155-217.
28. DTSA: Desk Top Spectrum Analyzer and X-ray Database, Standard Reference Data Program, National Institute of Standards and Technology, Gaithersburg, MD, 1995.
29. G. Cliff and G.W. Lorimer: *J. Microsc.*, 1975, vol. 103, pp. 203-07.
30. J.I. Goldstein, D.E. Newbury, P. Echlin, D.C. Joy, C. Fiori, and Eric Lifshin: in *Scanning Electron Microscopy and X-ray Microanalysis*, Plenum Press, New York, NY, 1984.
31. C. Nockolds, M.J. Nasir, G. Cliff, and G.W. Lorimer: *Proc. Inst. of Physics, Electron Microscopy and Analysis Group*, T. Mulvey, ed., Conf. Ser. No. 52, The Institute of Physics, London, 1979, pp. 417-20.
32. S.J.B. Reed: *Electron Microprobe Analysis*, Cambridge University Press, Cambridge, United Kingdom, 1975.
33. S.M. Allen: *Phil. Mag. A*, 1981, vol. 43, pp. 325-35.
34. D.B. Williams: *Practical Analytical Electron Microscopy in Materials Science*, Philips Electronic Instruments, Inc., Electron Optics Publishing Group, Mahwah, NJ, 1987.
35. B. Sundman, B. Jansson, and J.O. Andersson: *CALPHAD*, 1985, vol. 9, pp. 153-90.
36. ''Thermo-Calc, version K,'' Division of Computational Thermodynamics, Royal Institute of Technology, Stockholm, 1995.
37. B. Jansson: ''Evaluation of Parameters in Thermochemical Models Using Different Types of Experimental Data Simultaneously,'' TRITA-MAC-0234, Royal Institute of Technology, Stockholm, 1984.
38. Scientific Group Thermodata Europe, solution database, 1994.
39. G. Hägg: *Z. Kristallogr.*, 1934, vol. 89, pp. 92-94.
40. J. Sênateur and R. Fruchart: *C.R. Acad. Sci., Paris*, 1963, vol. 256, pp. 3114–17.
41. M.J. Duggin, D. Cox, and L. Zwell: *Trans. AIME*, 1966, vol. 236, pp. 1342-46.
42. J. Crangle and W. Sucksmith: *J. Iron Steel Inst.*, 1951, vol. 168, pp. 141-51.
43. H. Ino, K. Moriya, and E.F. Fujita: *Tetsu-to-Hagané*, 1968, vol. 54, pp. 34-47.
44. K.H. Jack: *J. Iron Steel Inst.*, 1951, vol. 169, pp. 26-36.
45. Y. Ohmori and S. Sugisawa: *Trans. JIM*, 1971, vol. 12, pp. 170-78.
46. Y. Ohmori: *Trans. JIM*, 1972, vol. 13, pp. 119-27.
47. Y. Imai, T. Kokura, and A. Inoue: *Tetsu-to-Hagané*, 1972, vol. 58, pp. 726-40.
48. A. Koreeda and K. Shimizu: *Proc. 5th Int. Conf. High Voltage Electron Microscopy*, Kyoto, Japan, 1977, Japan Electron Microscopic Society, Bunkyo-ku, Japan, 1977, pp. 611-14.
49. S. Nagakura, T. Suzuki, and M. Kusunoki: *Trans. JIM*, 1981, vol. 22, pp. 699-709.
50. S. Nagakura, Y. Horotsu, M. Kusunoki, T. Suzuki, and Y. Nakamura: *Metall. Trans. A*, 1983, vol. 14A, pp. 1025-31.
51. D. Meinhardt and O. Krisement: *Arch. Eisenhüttenwes*., 1962, vol. 33, pp. 493-99.
52. A.I. Gardin: *Sov. Phys.-Crystallogr.*, 1962, vol. 7, pp. 694-700.
53. F.H. Herbstein and J. Smuts: *Acta Crystallogr.*, 1964, vol. 17, pp. 1331-32.
54. K.A. Taylor, G.B. Olson, M. Cohen, and J.B. Vander Sande: *Metall. Trans. A*, 1989, vol. 20A, pp. 2749-65.
55. J. Mandel: *The Statistical Analysis of Experimental Data*, Dover Publications, Inc., New York, NY, 1964.
56. B. Sundman and J. Ågren: *J. Phys. Chem. Solids*, 1981, vol. 42, pp. 297-301.
57. M. Hillert and M. Jarl: *CALPHAD*, 1978, vol. 2, pp. 227-38.
58. J.B. Gilmour, G.R. Purdy, and J.S. Kirkaldy: *Metall. Trans.*, 1972, vol. 3, pp. 1455-64.
59. M. Hillert: in *The Mechanism of Phase Transformations in Crystalline Solids*, The Institute of Metals, London, 1969, pp. 231-47.
60. M.J. Aziz: *J. Appl. Phys.*, 1982, vol. 53, pp. 1158-68.
61. Z.-K. Liu, L. Höglund, B. Jönsson, and J. Ågren: *Metall. Trans. A*, 1991, vol. 22A, pp. 1745-52.
62. Z.-K. Liu and J. Ågren: *Metall. Trans. A*, 1991, vol. 22A, pp. 1753-59.
63. R.-H. Liarng: Ph.D. Thesis, Northwestern University, Evanston, IL, 1996.
64. C. Knepfler: Ph.D. Thesis, Northwestern University, Evanston, IL, 1994.
65. C.E. Campbell: Ph.D. Thesis, Northwestern University, Evanston, IL, 1997.
66. J.S. Langer and A.J. Schwartz: *Phys. Rev. A*, 1980, vol. 21, pp. 948-58.